

Gravity anomalies over the Central Indian Ridge between 3°S and 11°S, Indian Ocean: Segmentation and crustal structure

KIRANMAI SAMUDRALA¹, K A KAMESH RAJU^{1,*}  and P RAMA RAO²

¹*CSIR – National Institute of Oceanography, Dona Paula, Goa 403 004, India.*

²*Department of Geophysics, Andhra University, Visakhapatnam 530 003, India.*

**Corresponding author. e-mail: kamesh@nio.org*

High-resolution shipboard geophysical investigations along the Indian Ocean ridge system are sparse especially over the Carlsberg and Central Indian ridges. In the present study, the shipboard gravity and multibeam bathymetry data acquired over a 750 km long section of the Central Indian Ridge between 3°S and 11°S have been analysed to understand the crustal structure and the ridge segmentation pattern. The mantle Bouguer anomalies (MBA) and the residual mantle Bouguer anomalies (RMBA) computed in the study area have shown significant variations along the ridge segments that are separated by transform and non-transform discontinuities. The MBA lows observed over the linear ridge segments bounded by well-defined transform faults are attributed to the thickening of the crust at the middle portions of the ridge segments. The estimates of crustal thickness from the RMBA shows an average of 5.2 km thick crust in the axial part of the ridge segments. The MBA and relative RMBA highs along the two non-transform discontinuities suggests a thinner crust of up to 4.0 km. The most significant MBA and RMBA highs were observed over the Vema transform fault suggesting thin crust of 4 km in the deepest part of the transform fault where bathymetry is more than 6000 m. The identified megamullion structures have relative MBA highs suggesting thinner crust. Besides MBA lows along the ridge axis, significant off-axis MBA lows have been noticed, suggesting off-axis mantle upwelling zones indicative of thickening of the crust. The rift valley morphology varies from the typical V-shaped valley to the shallow valley floor with undulations on the inner valley floor. Segments with shallow rift valley floor have depicted well-defined circular MBA lows with persistent RMBA low, suggesting modulation of the valley floor morphology due to the variations in crustal thickness and the mantle temperature. These are supported by thicker crust and weaker lithospheric mantle.

1. Introduction

It has been well documented from the studies carried out over the slow-spreading ridges that gravity data can provide insights into the ridge segmentation, transform characteristics, crustal deformation, magma supply, and the dynamic processes

in the mantle. Gravity studies carried out over the segments of the Mid-Atlantic Ridge (MAR) have introduced the concept of mantle Bouguer anomaly (MBA) that provided insights into the mantle dynamics (Kuo and Forsyth 1988) and led to the identification of mantle upwelling zones characterised by bull's-eye MBA lows (Lin *et al.* 1990).

Keywords. Indian Ocean; Central Indian Ridge; geophysics; mantle Bouguer anomaly (MBA); residual mantle Bouguer anomaly (RMBA); multibeam bathymetry; mid-ocean ridge; transform fault.

Since then, many studies conducted over the slow-spreading ridges (Blackman and Forsyth 1991; Grindlay *et al.* 1991, 1992; Rommevaux *et al.* 1994; Sempere *et al.* 1993, 1995; Pariso *et al.* 1995; Lin and Morgan 1992; Tolstoy *et al.* 1993; Escartin and Lin 1995; Maia and Gente 1998; Gregg *et al.* 2007; Wang *et al.* 2011) have enhanced our understanding of the deep crustal processes at the mid-ocean ridges, mostly over the MAR.

High-resolution mapping efforts over the mid-ocean ridges, world-over, have revealed the fine-scale topographic fabric of the ridge crest region leading to the existence of new families of ridge axis discontinuities (MacDonald *et al.* 1991; Shaw 1992). These studies have shown that ridge axis discontinuities primarily divide the ridge into smaller segments with varied topographic expressions as a consequence of crustal accretion resulting from discrete spreading cells (MacDonald and Fox 1990; Shaw 1992; Sinton and Detrick 1992). Extensive investigations that are carried out over East Pacific Rise (EPR) and over the segments of MAR have provided insights into the segmentation pattern and accretionary processes of the fast and slow-spreading ridge systems (Macdonald *et al.* 1991; Scheirer and Macdonald 1993; Sempere *et al.* 1990, 1993; Smith and Cann 1993; Gente *et al.* 1995; Goslin and Triatnord Scientific party 1999). Recent investigations over the ultra-slow South West Indian Ridge (Sauter *et al.* 2001; Dick *et al.* 2003) and the Arctic Ridges (Cochran *et al.* 2003; Michael *et al.* 2003) have further enhanced our understanding of the architecture and accretionary processes of the slow-spreading mid-ocean ridges.

The Central Indian Ridge (CIR) north of the Indian Ocean triple junction is a slow-spreading mid-ocean ridge in the Indian Ocean with full-spreading rates of about 40 mm/yr. Basin-scale regional marine geophysical investigations dealing with the tectonic evolution of the Indian Ocean (Vine and Matthews 1963; McKenzie and Sclater 1971; Schlich 1982) and the plate reconstruction models (Royer and Sandwell 1989; DeMets *et al.* 1994) have provided a broad scale geometry of this ridge.

The ridge systems in the north Indian Ocean are less explored with respect to surveys with high-resolution mapping tools as compared to other ridge systems. Briaies (1995) and Kamesh Raju *et al.* (1997) provided initial results of detailed segment scale investigations carried out over parts of the CIR using the Gloria side scan and multibeam bathymetry, respectively. Segments of the slow spreading Carlsberg Ridge (CR) and the Central Indian Ridge (CIR) in the Indian Ocean have been studied in detail using the multibeam swath bathymetry (Kamesh Raju *et al.* 2008, 2012). The gravity study over the Rodriguez triple junction by

Honsho *et al.* (1996) is the only detailed gravity investigation using the shipboard gravity data over a part of the CIR.

Mantle upwelling and crustal accretion at slow-spreading ridges is believed to be a 3-D process that gives rise to significant segment-scale variations in crustal thickness with enhanced magma supply towards segment centres and less magma at segments ends (Kuo and Forsyth 1988; Lin *et al.* 1990; Chen 1992; Lin and Morgan 1992; Tolstoy *et al.* 1993; Canales *et al.* 2000; Hooft *et al.* 2000). In this paper, we present the first detailed analysis of the shipboard gravity data of the CIR between 3°S to 11°S, with an objective of providing insights into the crustal structure and segmentation. We have also used the multibeam data that has off-axis coverage extending up to magnetic anomaly 3 (4 Ma).

2. Marine geophysical data

The gravity data has been acquired during the 195 and 207 cruises of *RV Sagar Kanya* (July 2003 and August 2004). These are augmented with earlier published data of SK84 and the multibeam data of SK165 (Droliia *et al.* 2003; Droliia and DeMets 2005). Multibeam data from all the cruises have been merged and re-processed. The data covers about 750 km along the ridge with off-axis coverage of about 56 km on either side of the spreading axis, 100% insonification of the seafloor was achieved by three nautical mile spacing of the multibeam bathymetry tracks (figure 1) and gravity data was acquired along most of the multibeam tracks (figure 1). Gravity data was acquired by using the Bodenseewerk KSS30 sea gravity meter onboard the *RV Sagar Kanya*. An Integrated Navigation System (INS) with GPS MX4400 as the primary control has provided the navigation.

Gravity data has been processed and free-air gravity anomalies have been computed with the data reduced to the Marmugao base station. GMT (Wessel and Smith 1991) software was used for plotting and presentation of the data.

3. Gravity anomalies

3.1 Free-air gravity anomalies

The free-air gravity mimics the seafloor topography (figures 2 and 3). The multibeam bathymetry clearly depicts eight major ridge segments named I to P, the segments J, K and M are further divided into smaller segments of J1, J2, J3; K1, K2 and M1, M2 that are offset by non-transform discontinuities making up to 12 segments (figure 2). Segments I and J do not have the gravity data.

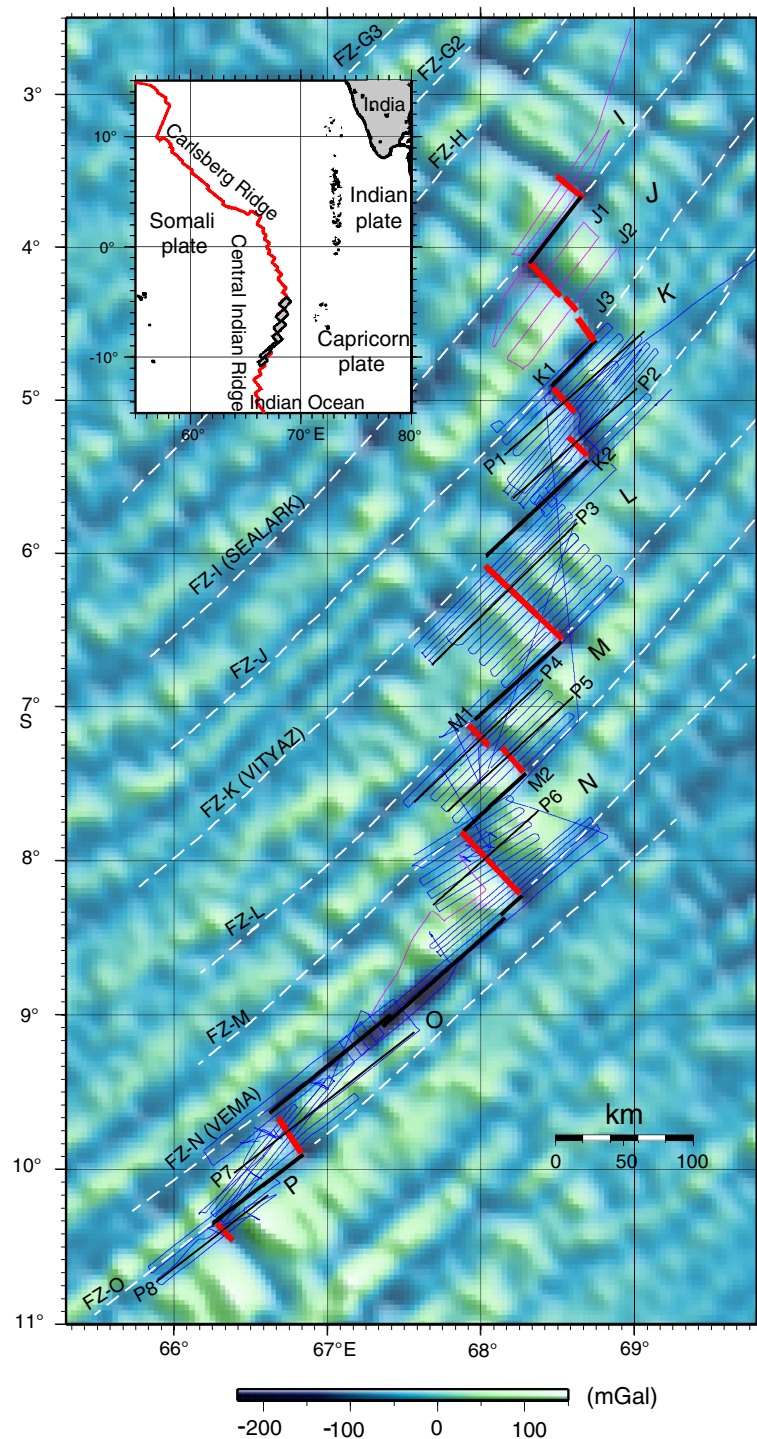


Figure 1. The Central Indian Ridge between 3°S and 11°S is depicted along with satellite-derived gravity image (Sandwell and Smith 1997). Thick red lines represent the ridge segments, these are named from I to O, thick black lines represent the transform faults. J1, J2, J3; K1, K2; M1, M2 are the sub-segments of segments J, K and M, respectively. Fracture zones are indicated with white dashed lines. Thin blue lines represent the ship-tracks along which gravity and multibeam bathymetry data have been acquired, thin red lines indicate the tracks along which only multibeam data is available. Lines labelled as P1 to P8 are the locations of the select profiles across the ridge segments. Inset indicates the Carlsberg and Central Indian Ridges in the Indian Ocean, and shaded box represent the study area.

The free-air gravity shows these segments with distinct gravity low along the ridge axis reflecting the rift valley and with off-axis highs and lows corresponding to the ridge parallel topographic highs and lows (figure 3). There are anomalous zones

superimposed on this general pattern arising due to the dominant subsurface density variations. Such features are noticed at the ridge-transform discontinuities and along the middle of the segment L, where the rift valley almost disappears. The Vema

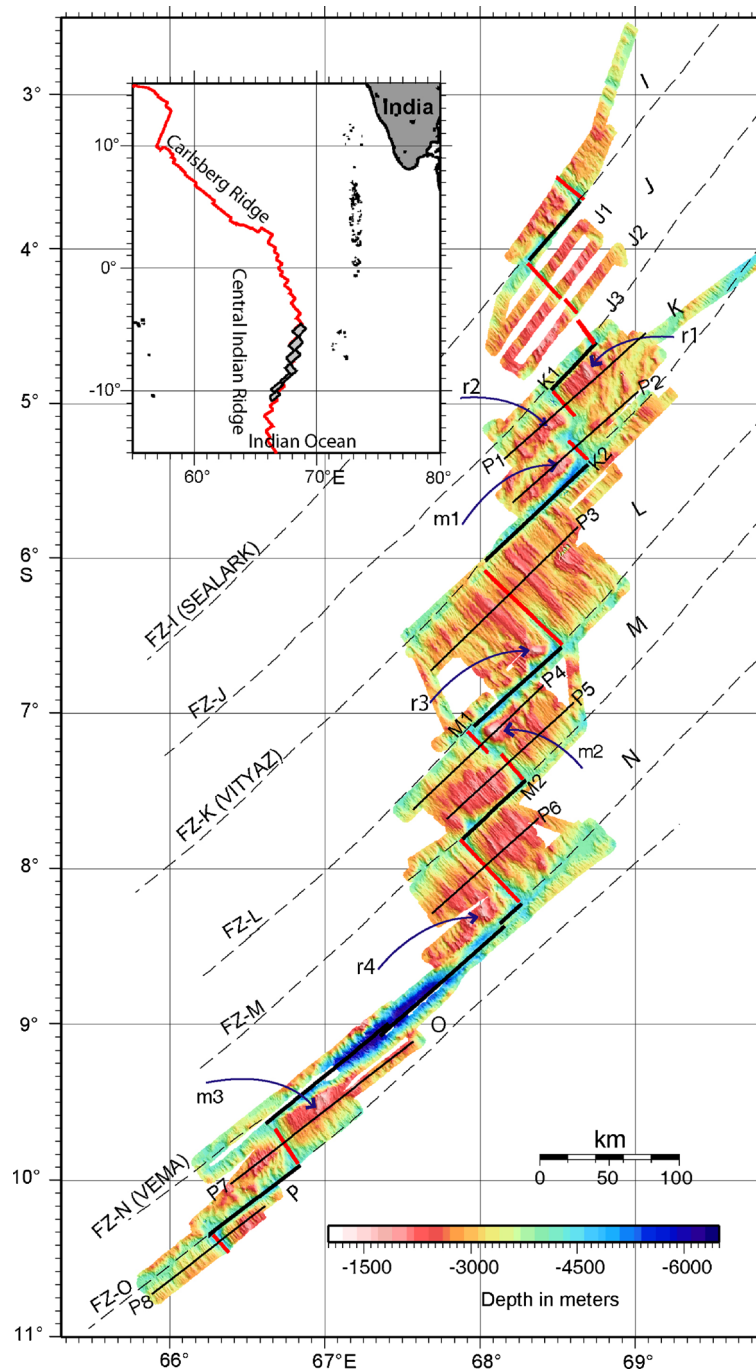


Figure 2. Multibeam bathymetry map of a section of the Central Indian Ridge. The other notations are same as in figure 1. Identified megamullion structures are labelled as m1, m2 and m3; r1–r4 represent identified ridge-transform intersection highs (modified after Kamesh Raju *et al.* 2012).

transform marking the deepest (6350 m) region of the survey area has a free-air low of -75 mGal (figure 3). The absence of gravity data in the region south-west of segment N (figure 1) has caused erroneous extrapolation of free-air anomalies, thereby adversely affecting further computations. Hence, this region has been masked and not used in interpretations.

In order to gain insights from the deeper subsurface layers, we have computed the mantle Bouguer anomaly (MBA) (figure 4) and the residual mantle Bouguer anomaly (RMBA) (figure 5)

from the free-air gravity anomaly by following the procedure of Prince and Forsyth (1988) and Kuo and Forsyth (1988) and are described in the sections below. Table 1 summarizes the values of parameters assumed in these computations.

3.2 Mantle Bouguer anomalies

We used the spectral method of Parker (1972) to calculate the mantle Bouguer anomaly by subtracting the predicted attractions of the water-crust,

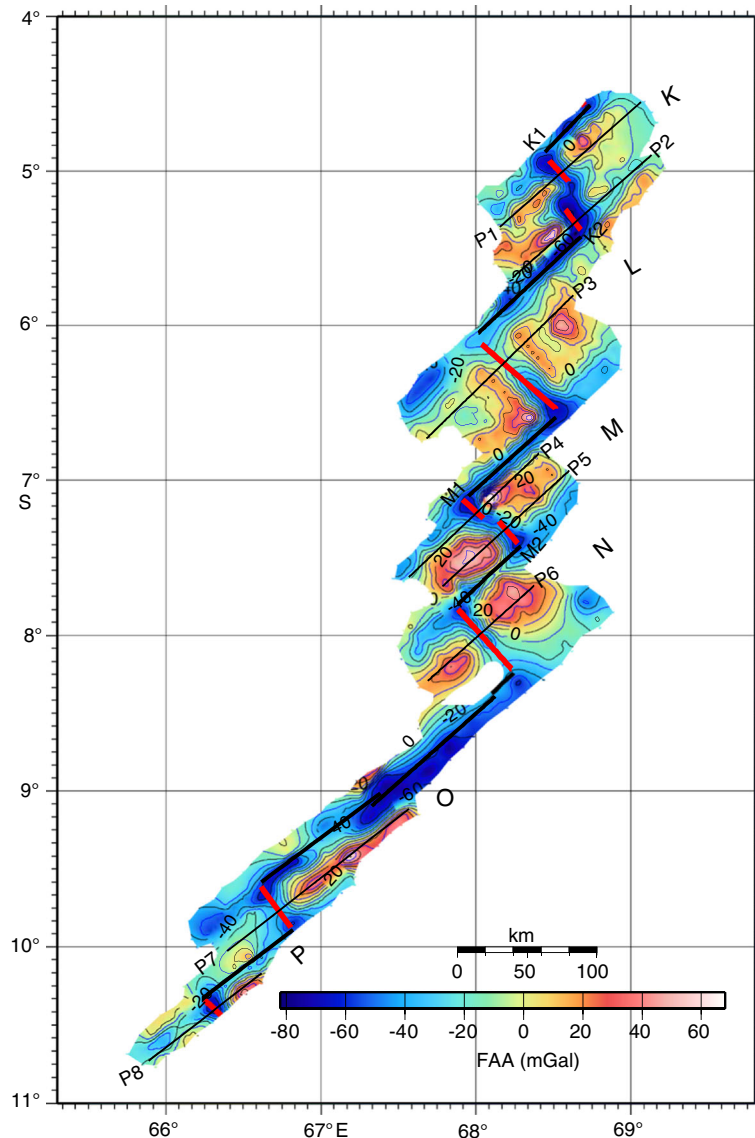


Figure 3. Free-air gravity anomaly map (contour interval 10 mGal) of the surveyed region. The other notations are same as in figure 1.

crust-mantle interfaces from the free-air anomaly assuming a constant reference crustal thickness of 6 km. It is a reasonable global average value for the oceanic crustal thickness (Spudich and Orcutt 1980). A Taylor's series expansion of powers of the Fourier transform of the topography was applied as for Parker's method. The non-linear nature of the gravitational attraction due to the topographic relief has been taken into account by considering the first three terms of the Taylor's series (Kuo and Forsyth 1988). We assumed the densities of water, crust, and mantle to be 1030 and 2700, and 3330 kg/m³, respectively (Kuo and Forsyth 1988; Wang *et al.* 2011). Thus, the MBA map depicts the variations in the density of the crust or mantle and also the departures from the assumed constant thickness of the crust. The mantle Bouguer anomalies varied from -85 to 80 mGal. The MBA lows are

observed at the middle of all six major spreading segments (figure 4).

3.3 Residual mantle Bouguer anomaly

The RMBA was calculated by removing the effects of lithospheric cooling with age and heat conduction across the ridge from the MBA. The thermal structure was calculated from 0 to 100 km depth using the age grid and a simple 1-D plate cooling model (Turcotte and Schubert 2002) with temperatures of $T_s = 0^\circ\text{C}$ at the surface and $T_m = 1350^\circ\text{C}$ at 100 km depth (table 1). The thermal structure was then converted into a 3D density grid using the thermal expansion equation, $\Delta\rho = (T_0 - T)\alpha\rho_0$, where T_0 and ρ_0 are reference temperature and density, respectively and α is the

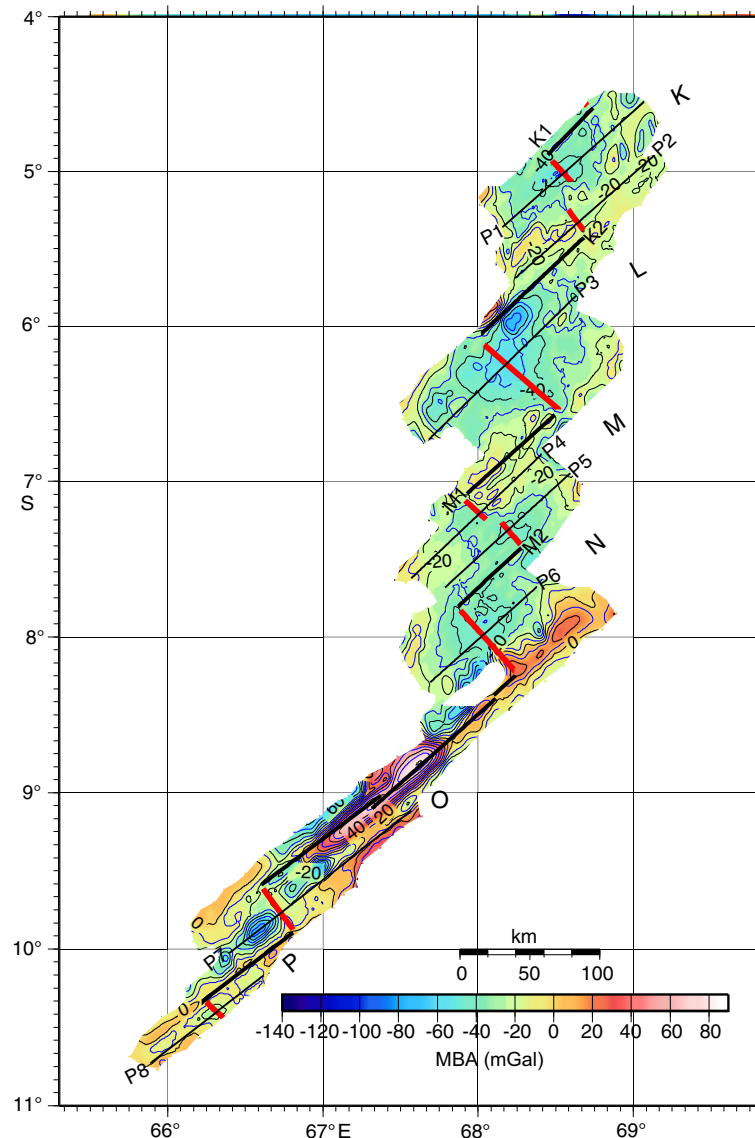


Figure 4. Mantle Bouguer anomaly (MBA) map (contour interval 10 mGal) of the surveyed region. Note the MBA lows over all the segments and prominent high over the Vema transform fault. The other notations are same as in figure 1.

thermal diffusivity constant. We used $T_0 = 1350^\circ\text{C}$ and $\rho_0 = 3330\text{ kg/m}^3$ (c.f. Kuo and Forsyth 1988).

The free-air, MBA and RMBA profiles across the segments K1, K2, L, M1, M2, N, O and P are presented along with the bathymetry (figure 6). The variations of free-air, MBA, RMBA and depth along selected profiles over different segments show (figure 6) rift valley configuration and the systematic variation of gravity signature. Bathymetry shows well-defined rift valley along all the segments.

The free-air gravity reflects the major topographic features (figure 7a, b). While the MBA shows a distinct low over the segment K1 (figure 7c), the RMBA shows relative high at the ridge-transform intersection (RTI) (figure 7d). Along the segment L, the rift valley shallows to about 2743 m and almost disappears (figure 8a) and

the free-air gravity follows the seafloor topography (figure 8b). Segment L shows well-defined near circular MBA low of -58 mGal (figure 8c). Further, an off-axis low of -75 mGal is observed towards north and east of the ridge axis (figure 8c). This is anomalous, a similar low adjacent to a pronounced low on the ridge axis was also observed north of ridge4 MAR (figure 6, Kuo and Forsyth 1988). The circular MBA observed over segment L is similar to the bull's eye MBA low observed over MAR segments (Lin *et al.* 1990; Lin and Morgan 1992; Tolstoy *et al.* 1993). These were interpreted in terms of focussed magmatic accretion resulting in significant crustal thickness variations over the ridge segments. In the present study, the variations of depth, free-air gravity and MBA show shallowing of the spreading axis in the middle of the ridge segment L with an MBA

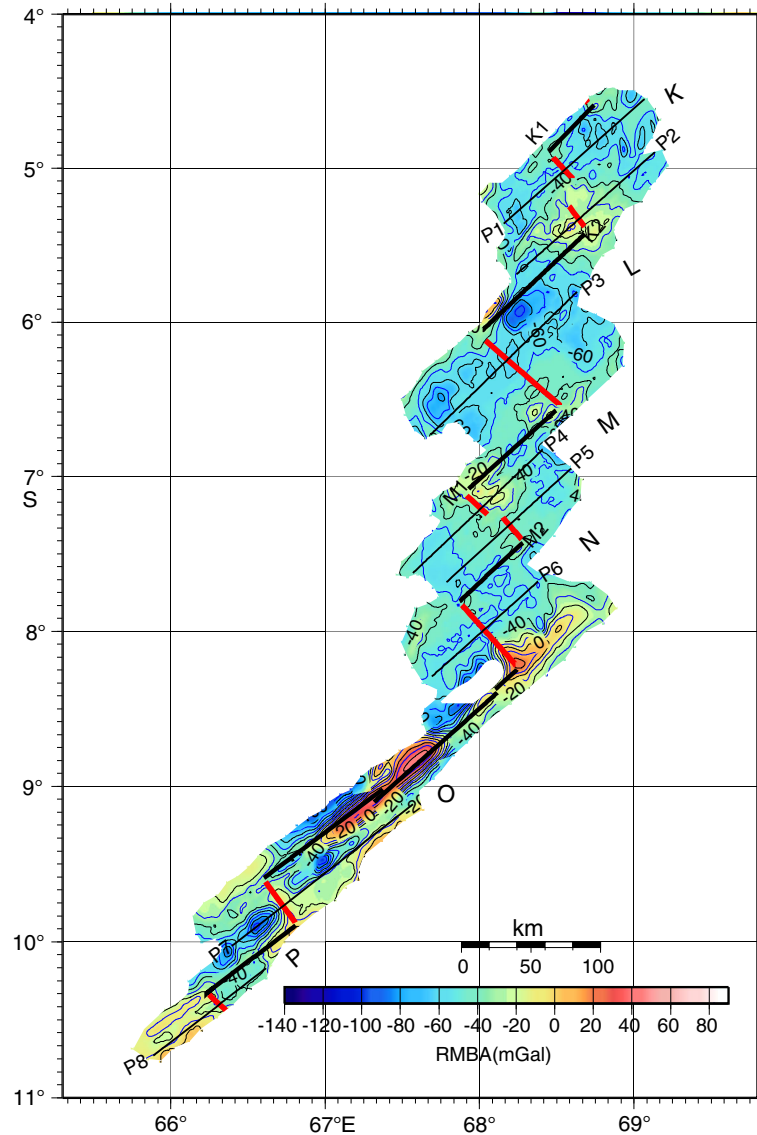


Figure 5. Residual mantle Bouguer anomaly (RMBA) map (contour interval 10 mGal) of the surveyed region. The other notations are same as in figure 1.

Table 1. Constants used in computations.

Symbol	Description, units	Value
ρ_w	Water density, kg m^{-3}	1.03×10^3
ρ_c	Crust density, kg m^{-3}	2.70×10^3
ρ_m	Mantle density, kg m^{-3}	3.33×10^3
H	Plate thickness, km	100
α	Volumetric coefficient of thermal expansion, $^{\circ}\text{C}^{-1}$	3×10^{-5}
T_s	Temperature at the surface of the plate, $^{\circ}\text{C}$	0
T_m	Temperature at the bottom of the plate, $^{\circ}\text{C}$	1350
ρ_0	Reference density, kg m^{-3}	3.33×10^3
T_0	Reference temperature, $^{\circ}\text{C}$	1350

low of -58 mGal (profile P3, figure 6). The MBA low observed here indicates along axis thickness variations in the crust. The well-developed rift valley and the observed relative MBA high

towards SE (figure 8c) suggest depleted accretion and crustal thinning at the transforms and at the ridge transform intersection (RTI) high. The increase in MBA away from the ridge axis and

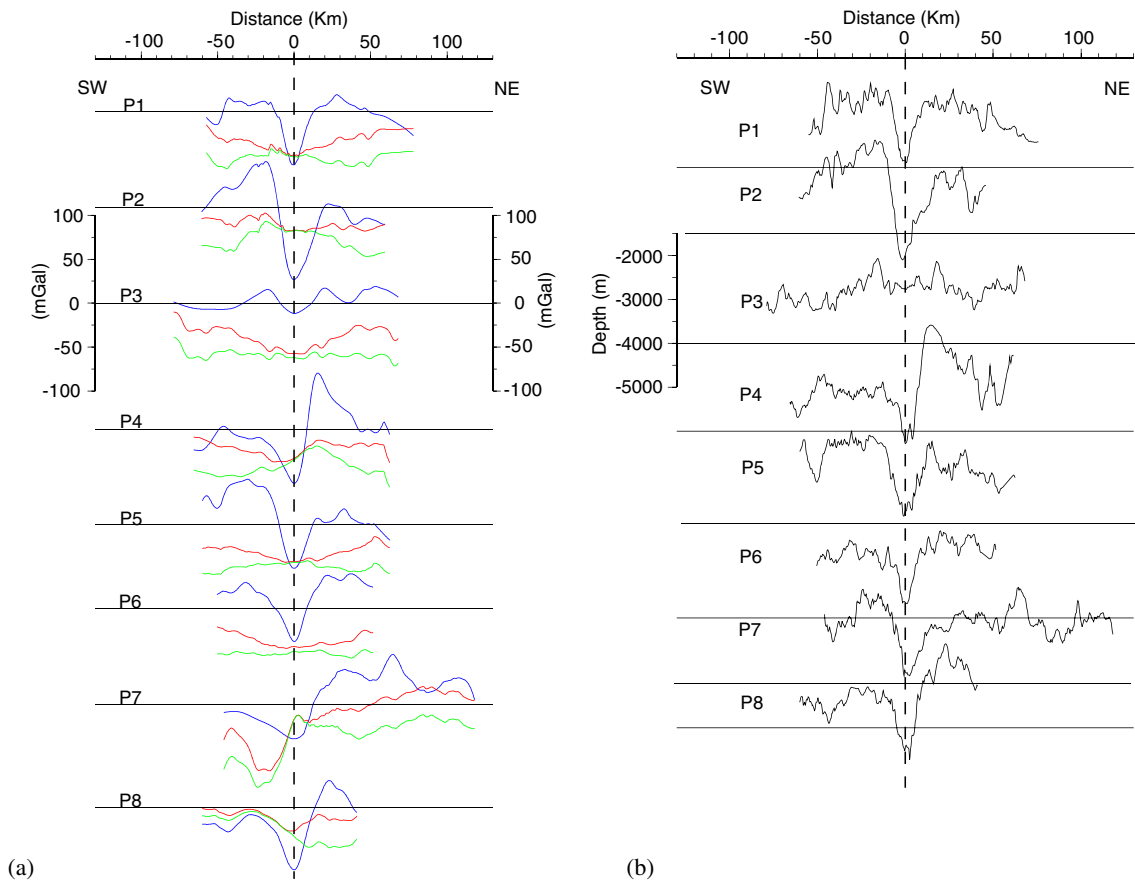


Figure 6. Profile plots along selected lines P1–P8 across the ridge segments extracted from the grid data. (a) Blue, red, and green lines indicate free-air anomaly, mantle Bouguer anomaly and the residual mantle Bouguer anomaly profiles, respectively. (b) Black indicate bathymetry. Note that prominent undulations observed over the rift valley along the profile P3. See figure 1 for the location of profiles P1–P8.

at the transforms were predicted along the MAR segments (Neumann and Forsyth 1993) using the iso-viscous, passive, flat plate model of Phipps Morgan and Forsyth (1988).

The section M has two short segments of M1 and M2 separated by a non-transform discontinuity (figure 9a, b). Prominent megamullion structure m2 (Kamesh Raju *et al.* 2012) is located to the east of segment M1. The megamullion structure is associated with MBA high (figure 9c), which extends well into the rift valley indicating significant crustal thinning. Segment N is a linear segment with a shallow rift valley at the centre of the segment (figures 10a and b). An MBA low is associated with the centre of the segment N (figure 10c). Segment O is a short linear segment (figure 11a, b). Off-axis MBA lows of -70 mGal corresponding to the flank topographic highs are observed along this segment (figure 11c).

The megamullion structures m1, m2, m3, and the RTI highs at r1–r4 (figure 2) show anomalous MBA signatures (figure 4). Megamullions m1 and m2 have significant relative MBA highs of -5 and -10 mGal. In contrast, m3, which is located off-axis along the Vema transform has an MBA of

-60 mGal. The RTI high r3 shows a relative MBA high of -10 mGal (figure 8c). The RTI highs r1 and r2, located off-axis show subdued relatively high MBAs (figure 7c). MBA highs at the megamullion structures m1 and m2 (figures 7c and 9c) indicate thin crust or no crust. Mantle rocks (serpentinised peridotites and gabbros) have been dredged from the locations of m1 and m2 (Kamesh Raju *et al.* 2012); whereas the megamullion observed at m3 shows an MBA low, the m3 is located off-axis of segment O (figure 11c). Segment P is a short ridge segment with a length of 24 km.

Another striking feature of the MBA map (figure 4) is the prominent MBA highs observed over the Vema transform fault offsetting the segments N and O. The Vema transform documents the deepest zone of 6350 m observed in the study area and has large offset of 250 km between the bounding ridge segments (figure 12a, b). The 80 mGal MBA high observed here (figure 12c) probably represent thin crust. The anomalous depth observed here is probably due to stretched and thinned crust within the Vema transform.

The MBA lows observed are subdued on the RMBA map and at places they diminish (figure 5).

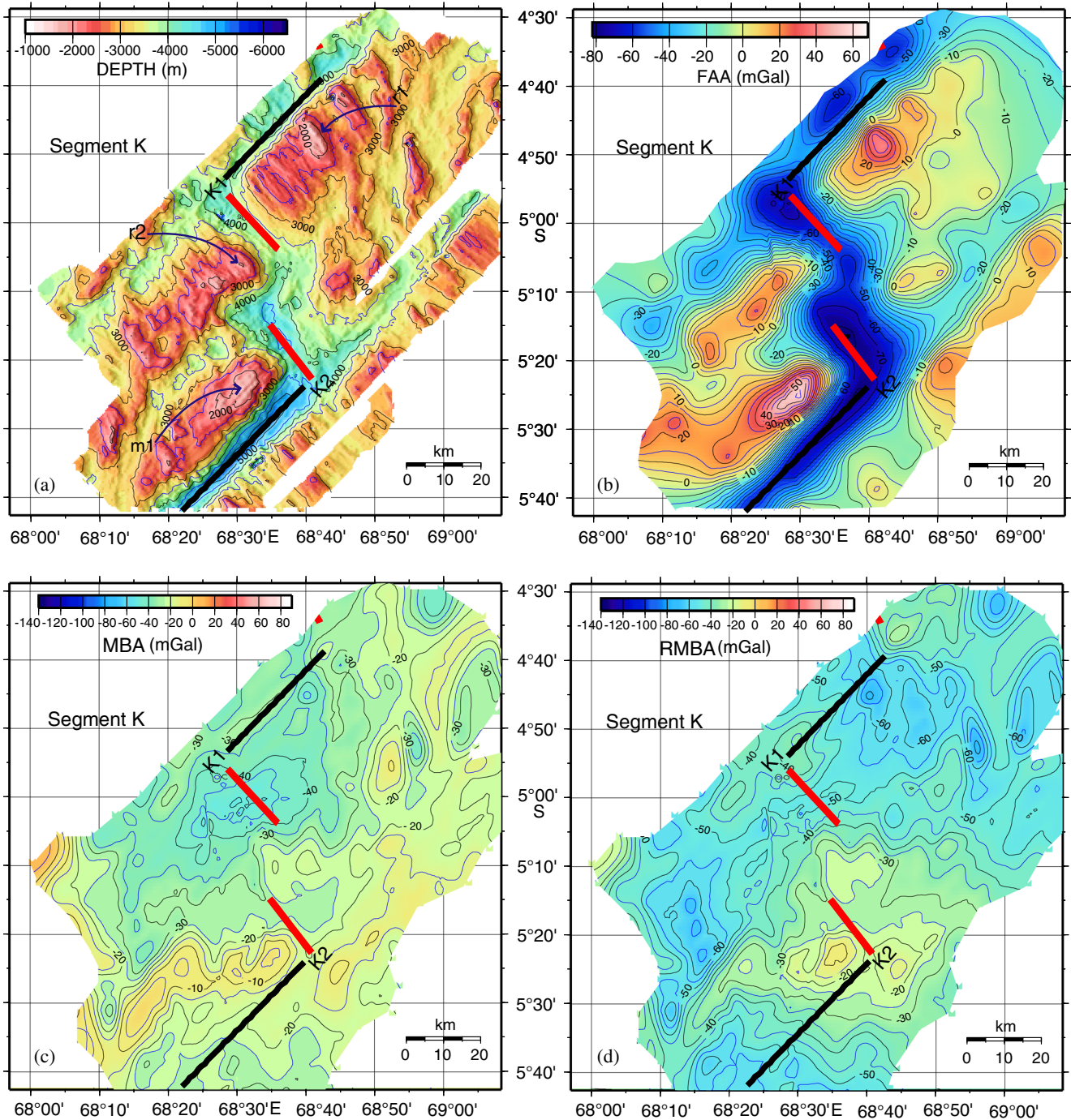


Figure 7. Enlarged colour-coded images along with contours of the segment K. (a) Bathymetry, (b) free-air anomaly, (c) mantle Bouguer anomaly, and (d) residual mantle Bouguer anomaly.

The MBA low observed on the segment L still remains in the RMBA map (figure 8d) indicating that the contribution of the crustal thickness variations is dominant on this segment. Relatively high RMBAs are observed over the megamullion structure m2 (figure 9d); whereas at other places, it can be assumed that the computed thermal structure is compensating the observed MBA lows. In general, RMBA highs are observed at the RTIs indicating thin crust. There are prominent RMBA highs observed at the southern end of the

segment N and O (figures 10d and 11d), and along the Vema transform. These highs probably represent thin crust at these locations. The most prominent RMBA high is along the Vema transform (figure 12d), where it is 40 mGal.

3.4 Crustal thickness

We performed 3-D inversion of RMBA for the computation of the Moho topography and crustal thickness beneath the CIR. For 3-D inversion, we

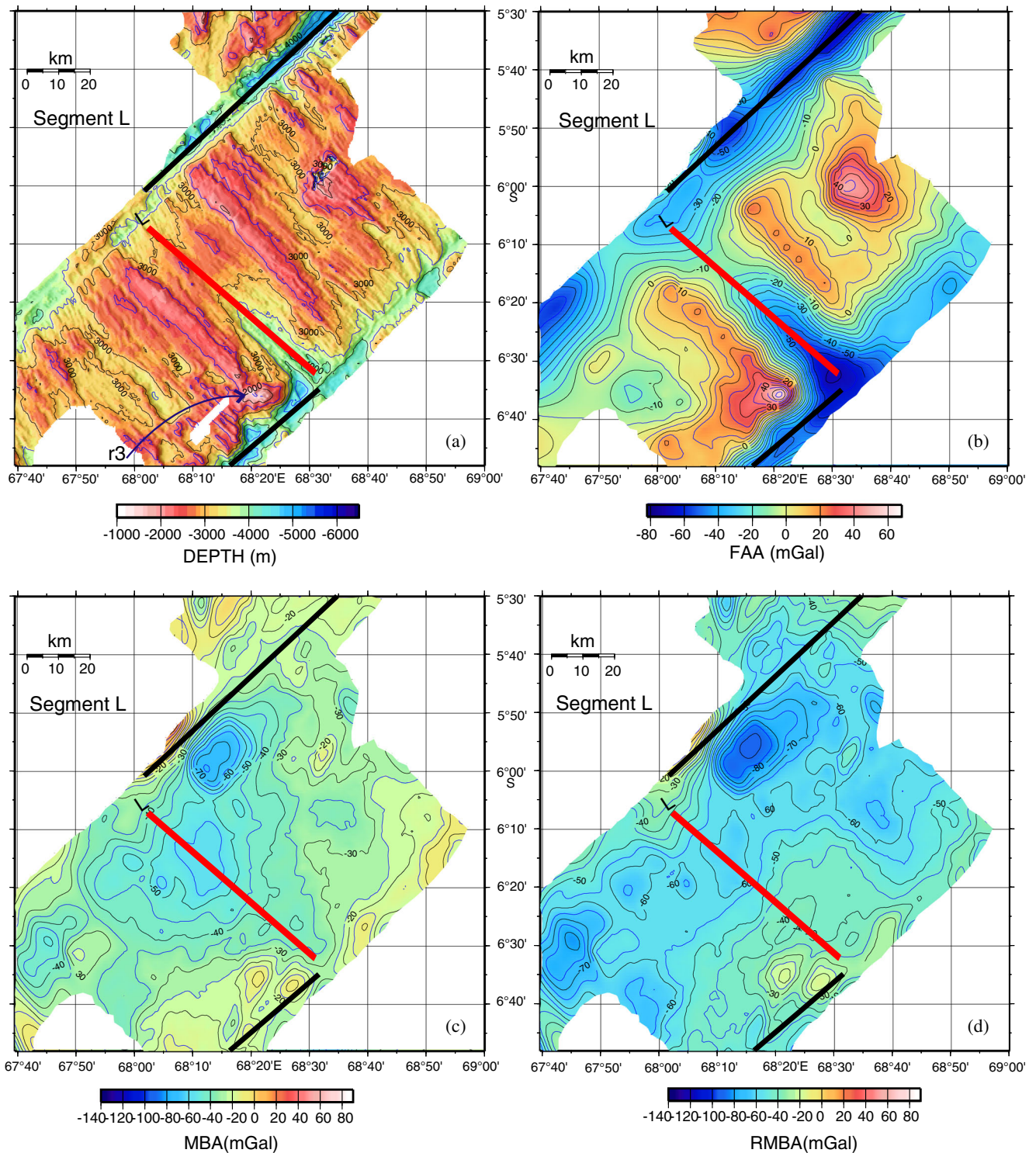


Figure 8. Enlarged colour-coded images along with contours of the segment L. (a) Bathymetry, (b) free-air anomaly, (c) mantle Bouguer anomaly, and (d) residual mantle Bouguer anomaly.

used Parker (1972) and Oldenburg (1974) iterative algorithm implemented in MATLAB by Ortiz and Agarwal (2005). This technique is based on Fast Fourier Transform (FFT). The parameters used for the inversion are the following: density contrast of 630 kg/m^3 (mantle density minus crust density) and a mean depth for the crust-mantle boundary

of 9.5 km (3.5 km is the average water depth and 6 km is the assumed crustal thickness). During the iterative procedure, the first term of the series is calculated using Parker's expression, and the resulting topography (in wavenumber domain) is filtered with cosine taper. Inverse FFT has been applied to the topography in wavenumber domain

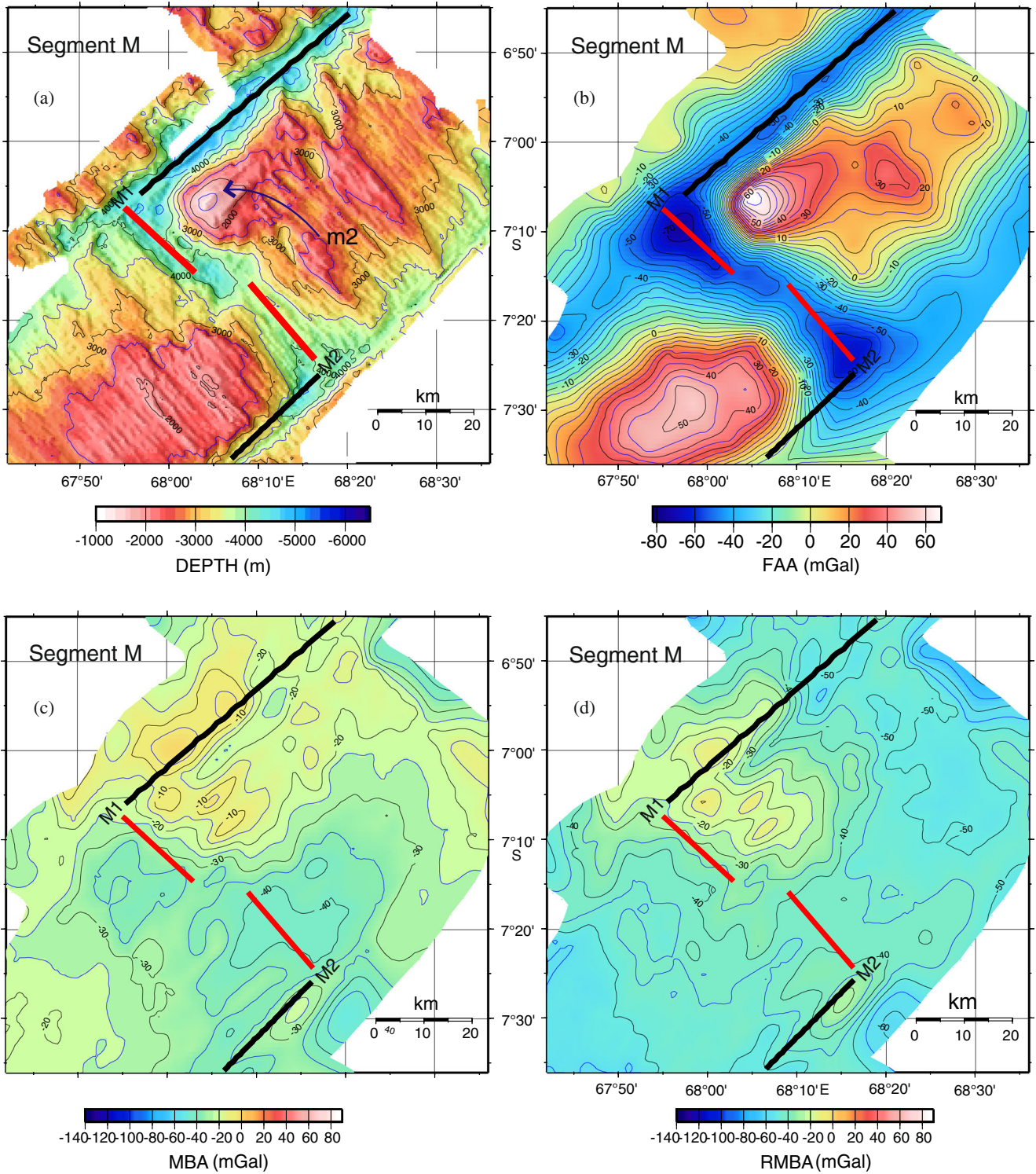


Figure 9. Enlarged colour-coded images along with contours of the segment M. (a) Bathymetry, (b) free-air anomaly, (c) mantle Bouguer anomaly, and (d) residual mantle Bouguer anomaly.

to obtain the Moho topography in the space domain. Cosine-taper with wavelengths between 35 and 25 km, and cut-off wavelengths shorter than 25 km, is applied. This is important to prevent amplification of shorter wavelength anomalies during the process and to enhance the convergence

in the iterative inversion. The crustal thickness is obtained by subtracting the bathymetry from the computed Moho topography (Alvey *et al.* 2008).

The resultant crustal thickness map (figure 13) depicts variations of crustal thickness along the ridge segments. We have extracted the along axis

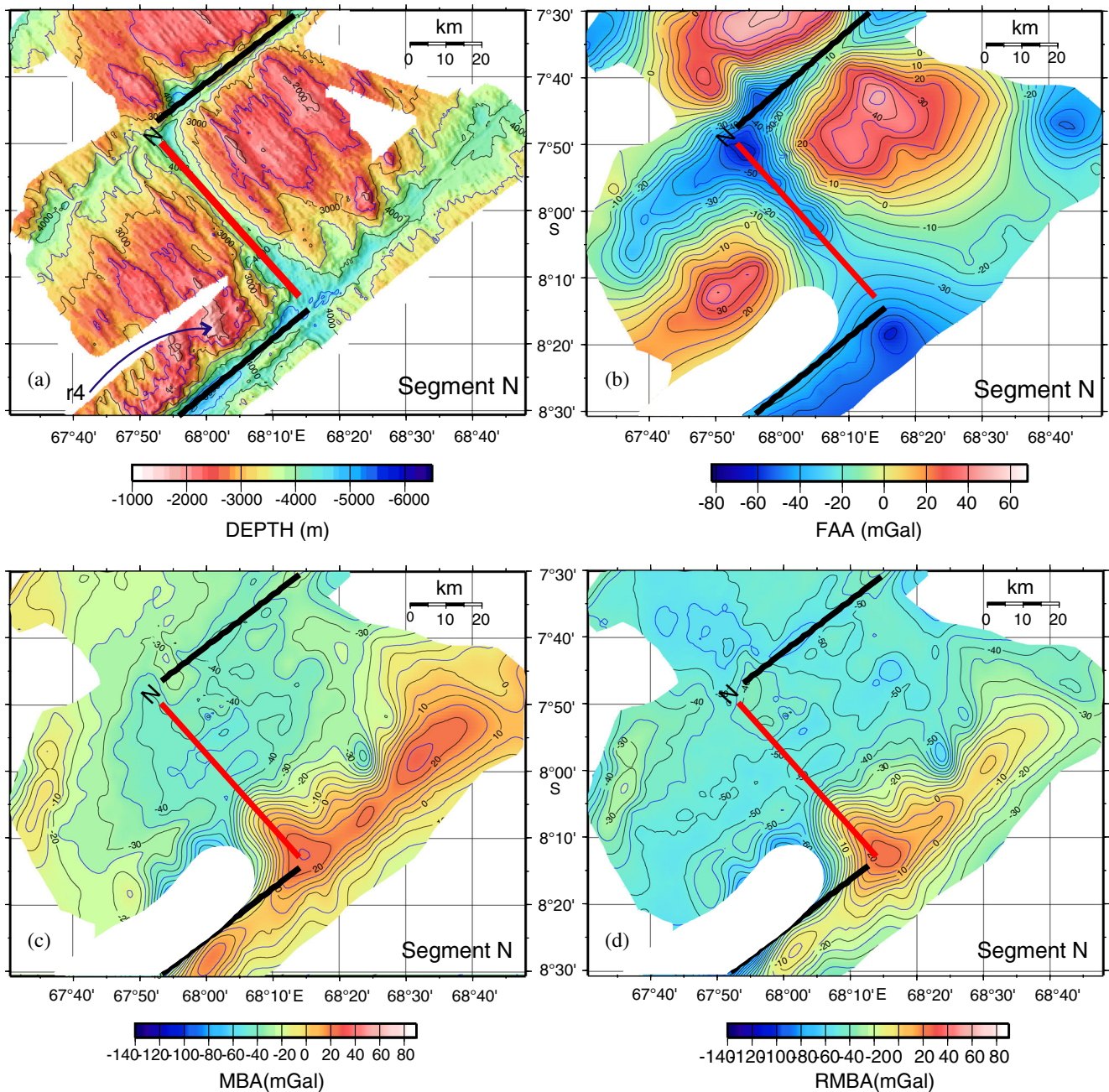


Figure 10. Enlarged colour-coded images along with contours of the segment N. (a) Bathymetry, (b) free-air anomaly, (c) mantle Bouguer anomaly, and (d) residual mantle Bouguer anomaly.

crustal thickness variations from the computed crustal thickness grid (figure 14). The segments K1 and K2 separated by non-transform discontinuity (NTD) have thicknesses of 5.1 and 5.8 km, respectively, with a thinning of the crust beneath the NTD to 4.0 km. Among the segments, a thick crust was observed beneath the segment L, the centre of segment L has a thickness of 7.8 km with the ends showing 1–2 km thinning resulting in a 6 km thick crust at the northern end and 5.8 km at the southern end. The segments M1 and M2 have crustal thicknesses of 5.1 and 5.3 km with

a thinning at the NTD to 4.8 km. The middle of segment N shows a thicker crust compared to the ends. The crust at the middle of segment N is 5.6 km thick, while the thickness at the northern end is 4.2 km and at the southern end is 5.0 km. Short segments O and P have 5.0 and 4.2 km thick crust, respectively. The average along the axis crustal thickness is 5.2 km, which is comparable with the along axis crustal thickness derived for the MAR (Lin *et al.* 1990). The longer linear segments L and N show thickening of the crust towards the middle of the segment. Thinning of the crust is seen

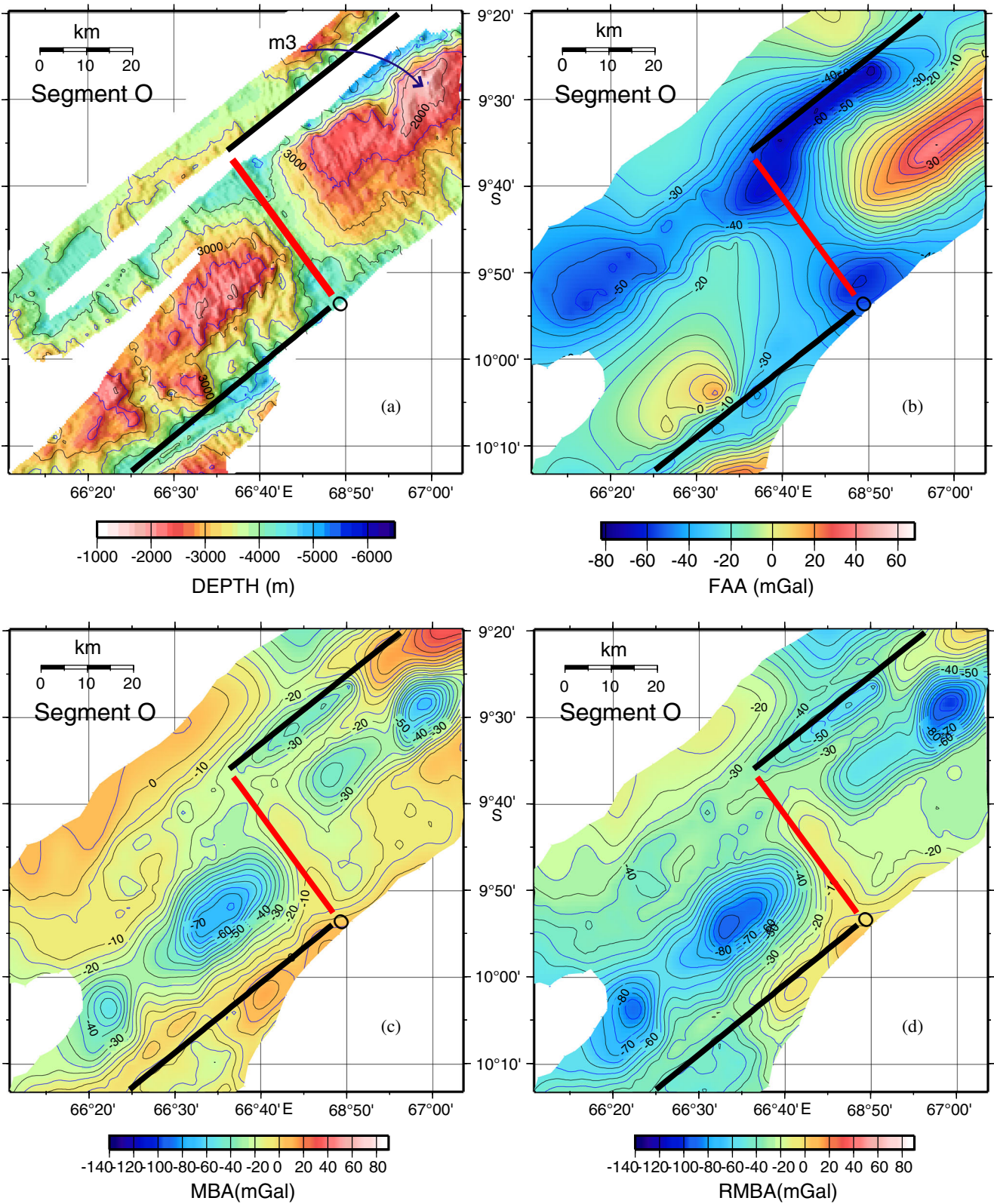


Figure 11. Enlarged colour-coded images along with contours of the segment O. (a) Bathymetry, (b) free-air anomaly, (c) mantle Bouguer anomaly, and (d) residual mantle Bouguer anomaly.

beneath the NTDs and the transform faults. The transform fault between K2 and L shows a thin crust of about 4 km and it is about 3 km along

the transform fault between L and M1. A thinner crust of about 3 km is observed over the transform fault between segments M2 and N. The Vema

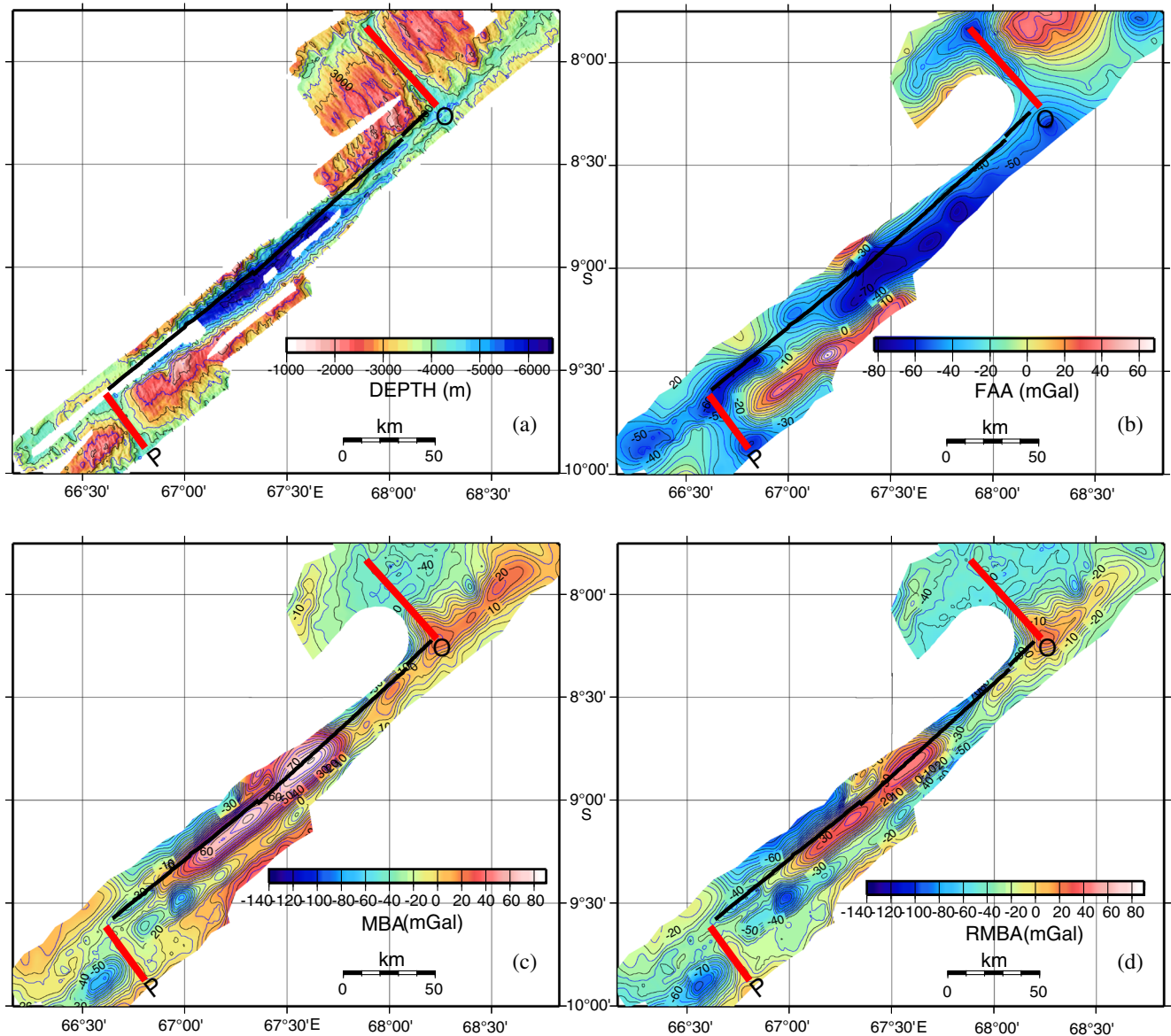


Figure 12. Enlarged colour-coded images along with contours of the Vema transform fault. (a) Bathymetry, (b) free-air anomaly, (c) mantle Bouguer anomaly, and (d) residual mantle Bouguer anomaly.

transform fault has a thin crust of about 4–5 km. The thickening of the crust away from the spreading axis is observed. The maximum thickness of crust, of 9–10 km, is observed on the flanks of segment L and adjacent to the Vema transform over the cold wall of the Vema transform fault.

3.5 Along axis variations

The along-axis profiles of bathymetry, free-air gravity, MBA and RMBA clearly brings out the segment boundaries and demarcate the transform faults (TFs) and non-transform discontinuities (NTDs) (figure 14). Segments K1, K2 and M1, M2 are

offset by prominent non-transform discontinuities. The along axis depth of the rift valley shows an inverse relationship with the MBA and RMBA as predicted. Segment L has the shallowest rift valley floor at 2743 m and the segment K2 has the deepest rift valley floor at 4680 m.

The segment L is conspicuous in its character compared to other segments. The rift valley almost disappears at the centre of this segment and is associated with prominent MBA low (figure 6). The maximum average measured full-spreading rate of 38 mm/yr was observed over the segment L (Kamesh Raju *et al.* 2012).

The average spreading rate of each segment suggests asymmetric spreading in terms of spreading

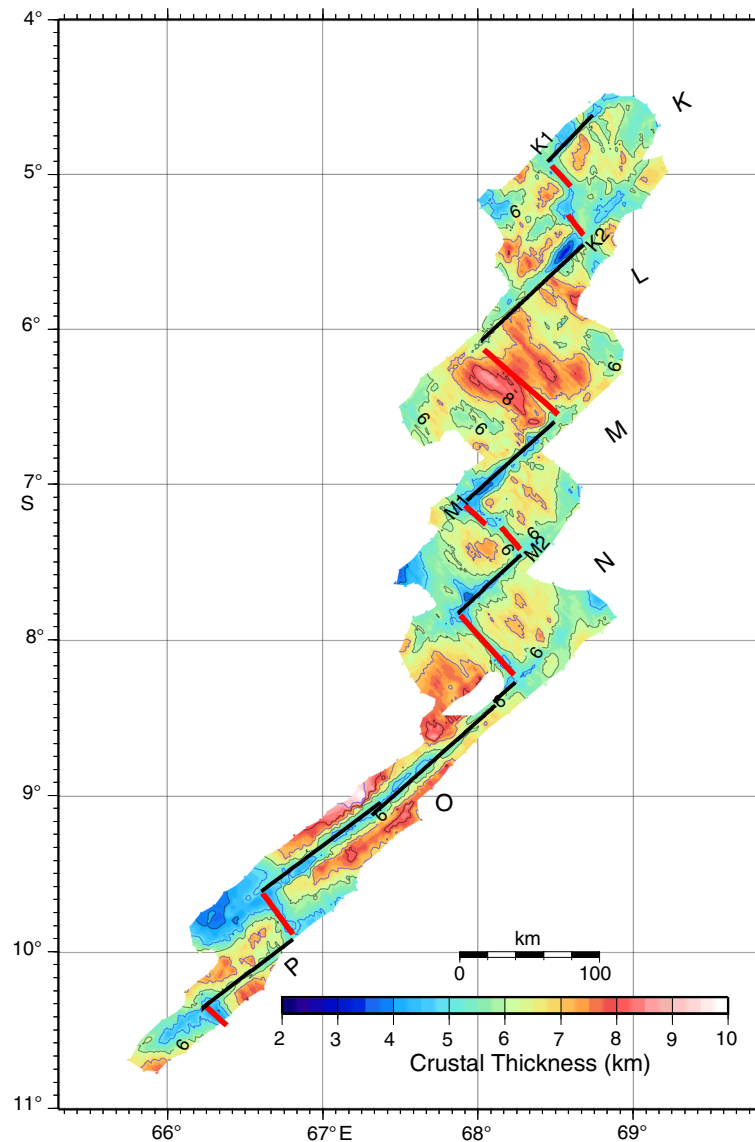


Figure 13. Crustal thickness computed from the residual mantle Bouguer anomaly; contour interval is 1 km.

rate derived from magnetic model studies and the average full-spreading rates varied from 26 to 38 mm/yr (Kamesh Raju *et al.* 2012). The deepest portion of the transform valley reaches a depth of 6350 m at the Vema transform.

3.6 Segments with non-transform discontinuity and linear segments

Segments K and M (figures 7 and 9) are characterised by prominent non-transform discontinuities with offsets of 17 and 7.5 km, respectively. The segments L, N and O (figures 8, 10, and 11) represent linear segments bounded by transform faults. The segment K1 has a narrow rift valley of about 8 km wide and a well-defined MBA low of -50 mGal. The segment K2, adjacent to it, has a wider rift valley of about 16 km and does not possess an MBA low. There is a prominent MBA high associated with

the megamullion structure m1, adjacent to segment K2 at the RTI. These highs are also reflected in the RMBA signature (figure 7d). In comparison, segments M1 and M2 (figure 9a) have a narrow rift valley of about 8 km and are marked by MBA lows. However, the MBA low corresponding to segment M1 is masked by the MBA highs associated with the megamullion structure m2 (figure 9c). It is interesting to note the ridge perpendicular lineation of MBA highs over the megamullion structure m2 (figure 9c). The RMBA map also shows prominent highs corresponding to the megamullion structure (figure 9d).

The linear segments L and N show prominent MBA lows over the portion of the ridge that is shallow and has narrow rift valley (figures 8 and 10). Small differences in crustal thickness and mantle temperatures appear to be adequate to produce a major change in lithospheric strength and axial

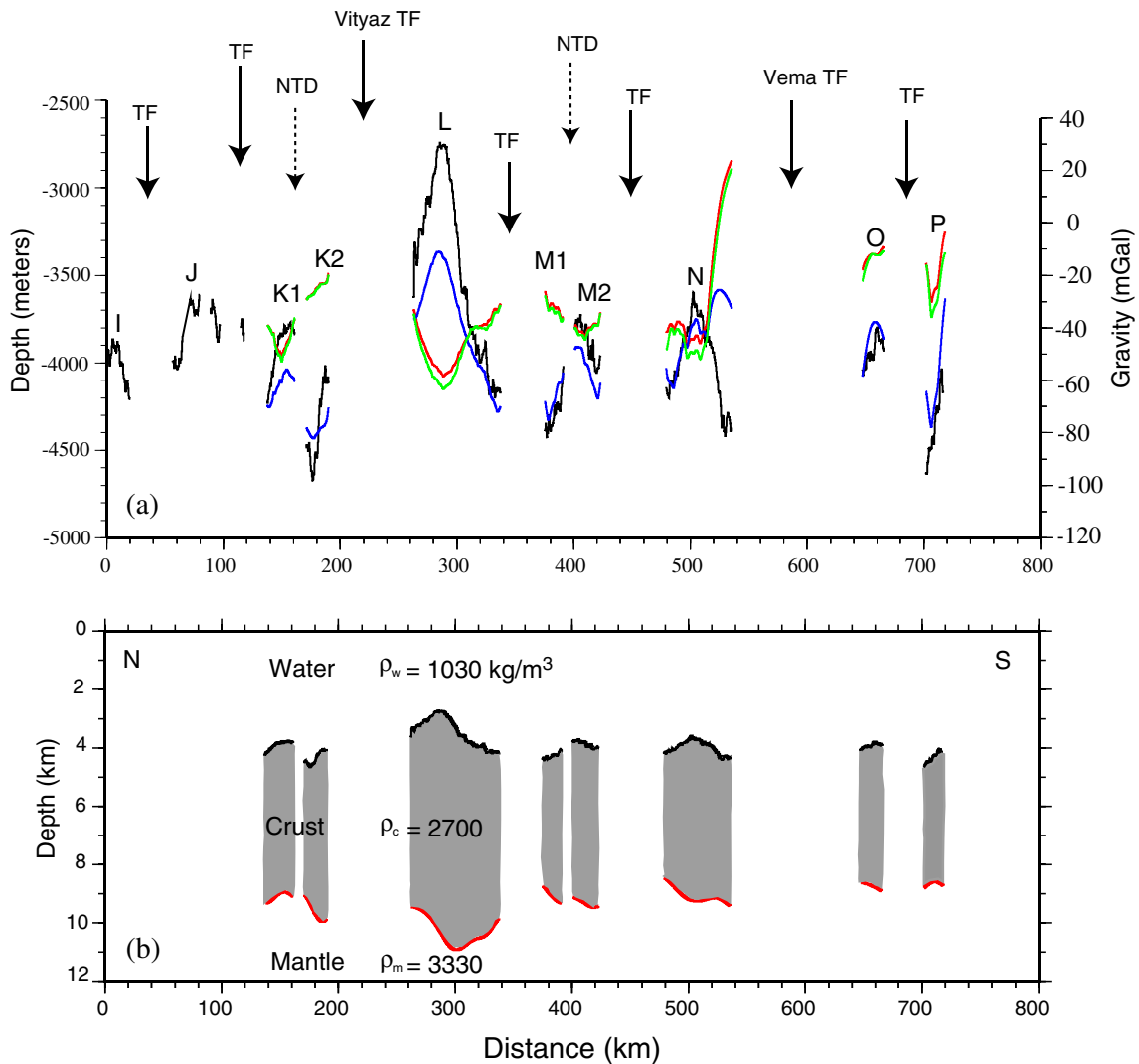


Figure 14. Along axis variations. (a) Black, blue, red and green lines represent bathymetry, free-air anomaly, mantle Bouguer anomaly and residual mantle Bouguer anomaly variations, respectively. Ridge segments, transform faults (TF), and non-transform discontinuities (NTD) are labelled. (b) Along-axis crustal thickness derived from computed crustal thickness grid. The zero on the distance axis is chosen arbitrarily at the starting of the segment I in the bathymetry map.

morphology as observed over the Juan de Fuca and Gorda ridges (Hooft and Detrick 1995). The variations seen in the rift valley configurations and the associated changes in the MBA and RMBA signatures observed over the segments of the present study also support this argument. The segment O is a short segment of 35 km having a rift valley width of 8 km and does not display an MBA low.

4. Discussion

The magma supply is considered to strongly affect local tectonics (Tapponnier and Francheteau 1978; Harper 1985; Karson 1987). Mantle Bouguer anomaly lows at the segment centres may either reflect hot, low-density crust or mantle, thicker crust or some combination of both (Lin *et al.* 1990). Magmatic and sparsely magmatic sections have

been identified over the CIR based on rift valley morphology and off-axis topographic fabric (Kamesh Raju *et al.* 2012). It is observed that the magmatic sections are associated with well-defined MBA lows, while the expression is subdued over the segments that are sparsely magmatic. The most pronounced MBA low is observed over the linear segment L. Here, the rift valley almost disappears leading to a shallow valley floor with closely spaced fault scarps (profile P3, figure 6). Theoretical models (Shaw and Lin 1994) suggest that decoupling of upper crust from the mantle by weak lower crust may occur at the segment centres. A consequence of this is a thin weak lithosphere at segment centre and a thick, strong lithosphere at segment ends (Escartin and Lin 1995). The thin lithosphere over the weak lower crust favours the formation of small closely spaced faults at the segment centres (Shaw 1992; Shaw

and Lin 1993). These fault scarps tend to be axis parallel (Escartin and Lin 1992) and this is evident at the centre of the segment L supported by the robust mantle upwelling. Whereas, the segment ends preferentially will have low angle faults at inside corners, where the mantle lithosphere is strongest and the lithospheric plates are sufficiently decoupled across the ridge axis offsets (Escartin and Lin 1995). The gravity signatures, the rift valley morphology and the RTI high configurations observed in the present study support these inferences. The off-axis MBA low observed towards the northern end of the segment L probably represents the crustal accretion at the transform flank due to local pooling of the melt that probably is related to the focussed upwelling at the segment centre. At present, we do not have any strong indicators to know how this lateral migration of magma from the segment centre to the off-axis takes place. The spreading rate along the segment L is the highest (Kamesh Raju *et al.* 2012) among the segments under study and the higher spreading rate could be a consequence of kinematics of plate separation. It has been observed, in general, that spreading centres with spreading rates less than 30–40 mm/yr are typically associated with 1–2 km deep, 15–30 km wide rift valley, while ridges with full-spreading rate faster than 60–70 mm/yr are associated with a 2–10 km wide, 200–300 m axial highs (MacDonald 1982). The CIR with a spreading rate of 26–38 mm/yr (Kamesh Raju *et al.* 2012) is a typical slow-spreading ridge, yet the segment L displays subdued rift valley morphology. The rift valley floor at segment L is only 650 m deep with respect to the valley walls and has closely spaced fault scarps marking minor undulations of 50 to 60 m and major undulations of 250–300 m (profile P3, figure 6). The inner valley floor has a width of 27 km. These morphological characters are typical of segment L, whereas the other segments have a deep rift valley typical of slow-spreading ridges (figure 6). This is attributed to the focused mantle upwelling with robust magma supply resulting in a thicker crust and hotter, weaker mantle lithosphere along segment L. The ridge crest morphology of segment L is distinctly different from the segment K to the north and segment M to the south. It has been observed that the ridge crest morphology is particularly sensitive to the changes in thermal structure and magma supply at intermediate spreading rates (Phipps Morgan and Chen 1993). In the case of CIR, the gravity signatures suggest that magma supply has modulated the ridge crest morphology along the segment L.

The second-order discontinuities or non-transform discontinuities (NTDs) are associated with a wide deformation zone with complex morphology and

tectonics and have a limited lifespan (Grindlay *et al.* 1991). The NTDs tend to change their orientation with time to become more parallel to the ridge and perpendicular to the spreading direction. In contrast, the transform discontinuities maintain the initial narrow strike-slip orientation (van Wijk and Blackman 2005). Further, it has been observed through model studies that the regions in line with the axes and the oblique deformed zone will experience thinning (van Wijk and Blackman 2005). We have observed a thin crust of 4.0 and 4.8 km at the NTDs between the segments K1, K2 and M1, M2, respectively. The NTDs observed between segments K1 and K2 and M1 and M2 are associated with MBA highs. The MBA high centred over the nodal basin between K1 and K2 is more pronounced. These MBA highs are also associated with relative RMBA highs and suggest crustal thinning. Taking an analogy of the segment L, the segments with NTDs can be suggested to have low magma supply, resulting in thinner crust and colder and stronger mantle lithosphere. The MBA and RMBA highs observed over the NTDs at segments K and M support this inference.

It has been observed that the RTIs are associated with positive RMBAs indicating thinning of the crust. Prominent among them are the megamullion structures observed at m1 and m2 and the RTI high r3 at the southern end of segment L. The megamullion structures in general show elevated MBA signatures (Blackman *et al.* 2009).

The transform faults, in general, have relatively high MBA values indicating a thin crust. The Vema transform has the highest MBA and associated RMBA highs in the middle of the transform zone (figure 12c, d); this zone also has the deepest seafloor. Studies by Kuo and Forsyth (1988); Lin *et al.* (1990); Lin and Morgan (1992) and Detrick *et al.* (1995) have attributed positive RMBA along the slow-slipping transform faults to diminished crustal accretion at the ends of the segment and consequently, the transform fault domain. The MBA and RMBA variations observed on the flanks of the transform are attributed to the crustal thickness variations (Gregg *et al.* 2007). The mantle lithosphere at the Vema transform can be expected to be strong with thin crust, as revealed by MBA and RMBA highs (figure 12c, d). In a similar tectonic setting, seismic experiments (Detrick and Purdy 1980) have shown extremely thin crust within the Kane FZ trough.

In general, the crustal thickness along the segments varied, with thick crust near the middle of the segments and thin crust near the segment ends (figure 14b). Along the slow-spreading MAR, it has been observed that the magnitude of the along-axis variation in crustal thickness is proportional

to the segment length and the size of the adjacent ridge offset (Detrick *et al.* 1995). The variation in the along axis thickness along the longer segments L and N are more prominent than elsewhere, and this segment scale crustal heterogeneity is similar to that observed over MAR. It has also been shown that the magnitude of along axis variation in MBA is proportional to the segment length with longest segments having largest MBA (Lin *et al.* 1990).

5. Conclusions

Based on morphology, the 750 km long section of the CIR is broadly segmented into twelve ridge segments that are displaced by seven transform faults and two non-transform discontinuities. Both the transform faults and the non-transform discontinuities are characterised by a thin crust.

All the linear segments of the CIR that are bounded by transform faults display MBA lows, indicating thick crusts at the middle of the segments. The most prominent MBA low was observed over the segment L, where the rift valley becomes less prominent. The inner valley floor across the segment L has closely spaced fault scarps suggesting modulation of the valley floor morphology due to the variation in crustal thickness and the mantle temperature.

The RTI highs and the identified megamullion structures, with the exception of off-axis highs, in general, display prominent MBA highs suggesting thinner crust and stronger mantle lithosphere. The most prominent MBA and RMBA highs were observed over the Vema transform. The MBA and RMBA highs are attributed to a thin crust of about 4 km over the Vema transform, where a maximum depth of 6350 m has been documented.

The average along the axis crustal thickness computed from RMBA is 5.2 km. The longer linear segments L and N have shown up to 7.8 km thickening of the crust towards the middle of the segment.

Acknowledgements

We thank Dr S W A Naqvi, Director, CSIR – National Institute of Oceanography, Goa, for the encouragement and support given to carry out this study. We are thankful to Mohammad Ismaiel for his help in the computation of crustal thickness. We thank the anonymous reviewers for the constructive comments and corrections, and the associate editor for encouragement. The data were acquired under the Ridge project, funded by the CSIR-Network program. Data analysis and interpretation were carried out under the GEOSINKS,

CSIR-Network program of XII plan. We acknowledge the help rendered by the ship crew and colleagues during the acquisition of the data. This is CSIR-N.I.O. contribution no. 5934.

References

- Alvey A, Gaina C, Kuszniir N J and Torsvik T H 2008 Integrated crustal thickness mapping and plate reconstruction for the high Arctic; *Earth Planet. Sci. Lett.* **274** 310–321.
- Blackman D K and Forsyth D W 1991 Isostatic compensation of tectonic features of the Mid-Atlantic Ridge: 25–27°30'S; *J. Geophys. Res.* **96** 11,741–11,758.
- Blackman D K, Canales J P and Harding A 2009 Geophysical signatures of oceanic core complexes; *Geophys. J. Int.* **178** 593–613.
- Briais A 1995 Structural analysis of the segmentation of the Central Indian Ridge between 20°30' and 25°30'S (Rodriguez Triple Junction); *Mar. Geophys. Res.* **17** 431–467.
- Canales J P, Detrick R S, Lin J, Collins J A and Toomey D R 2000 Crustal and upper mantle seismic structure beneath the rift mountains and across a non-transform offset at the Mid-Atlantic Ridge (35°N); *J. Geophys. Res.* **105** 2699–2719.
- Chen Y J 1992 Oceanic crustal thickness versus spreading rate; *Geophys. Res. Lett.* **19** 753–756.
- Cochran J R, Kurrus G J, Edwards M H and Coakley B J 2003 The Gakkel Ridge: Bathymetry, gravity anomalies and crustal accretion at extremely slow spreading rates; *J. Geophys. Res.* **108**(B2), doi: [10.1029/2002JB001830](https://doi.org/10.1029/2002JB001830).
- DeMets C, Gordon R G and Vogt P 1994 Location of the Africa–Australia–India triple junction and motion between the Australian and Indian plates: Results from an aeromagnetic investigation of the central Indian and Carlsberg ridges; *Geophys. J. Int.* **119** 893–930.
- Detrick R S and Purdy G M 1980 The crustal structure of the Kane fracture zone from seismic refraction studies; *J. Geophys. Res.* **85** 3759–3777.
- Detrick R S, Needham H D and Renard V 1995 Gravity anomalies and crustal thickness variations along the Mid-Atlantic Ridge between 33°N and 40°N; *J. Geophys. Res.* **100** 3767–3787.
- Dick H J B, Lin J and Schouten H 2003 An ultraslow spreading class of Ocean ridge; *Nature* **426** 405–412.
- Drobia R K and DeMets C 2005 Deformation in the diffuse India–Capricorn–Somalia triple junction from a multi-beam and magnetic survey of the northern Central Indian ridge, 3°S–10°S; *Geochem. Geophys. Geosyst.* **6** Q09009.
- Drobia R K, Iyer S D, Chakraborty D, Kodagali V N, Dwijesh Ray, Misra S, Andrade R, Sarma K V L N S, Rajasekhar R P and Mukhopadhyay R 2003 The Northern Central Indian Ridge: Geology and tectonics of fracture zones – dominated spreading ridge segments; *Curr. Sci.* **85**(3) 290–298.
- Escartin J and Lin J 1992 Morfoestructura de la dorsal medio-Atlantica entre 24°N y 30°N (Morphotectonics of the Mid-Atlantic Ridge, 24°N–30°N); *Acta Geologica Hispanica* **27** 33–49.
- Escartin J and Lin J 1995 Ridge offsets, normal faulting, and gravity anomalies of slow spreading ridges; *J. Geophys. Res.* **100** 6163–6177.
- Gente P, Pockalny R A, Durand C, Deplus C, Maria M, Ceuleneer G, Mevel C, Cannat M and Laverne C 1995 Characteristics and evolution of the segmentation of the

- Mid-Atlantic Ridge between 20°N and 24°N during the last 10 million years; *Earth Planet. Sci. Lett.* **129** 22–71.
- Gregg P M, Lin J, Behn M D and Montesi L G 2007 Spreading rate dependence of gravity anomalies along oceanic transform faults; *Nature* **448**, doi: [10.1038/nature05962](https://doi.org/10.1038/nature05962).
- Grindlay N R, Fox P J and MacDonald K C 1991 Second-order ridge axis discontinuities in the South Atlantic: Morphology, structure, and evolution; *Mar. Geophys. Res.* **13** 21–49.
- Grindlay N R, Fox P J and Vogt P R 1992 Morphology and tectonics of the Mid-Atlantic Ridge (25°–27°30'S) from SeaBeam and magnetic data; *J. Geophys. Res.* **97** 6983–7010.
- Goslin J and Triatnord Scientific Party 1999 Extent of Azores plume influence on the Mid-Atlantic Ridge north of hotspot; *Geology* **27** 991–994.
- Harper G D 1985 Tectonics of slow-spreading mid-ocean ridges and consequences of a variable depth to the brittle/ductile transition; *Tectonics* **4** 395–409.
- Honsho C, Tamaki K and Fujimoto H 1996 Three-dimensional magnetic and gravity studies of the Rodriguez Triple Junction in the Indian Ocean; *J. Geophys. Res.* **101** 148–227.
- Hooft E E E and Detrick R S 1995 Relationship between axial morphology, crustal thickness and mantle temperature along the Juan de Fuca and Gorda Ridges; *J. Geophys. Res.* **100** 22,499–22,508.
- Hooft E E E, Detrick R S, Toomey D R, Collins J A and Lin J 2000 Crustal thickness and structure along three contrasting spreading segments of the Mid-Atlantic Ridge, 33.5°–35°N; *J. Geophys. Res.* **105** 8205–8226.
- Kamesh Raju K A, Ramprasad T and Subrahmanyam C 1997 Geophysical investigations over a segment of the Central Indian Ridge, Indian Ocean; *Geo-Marine Lett.* **17** 195–201.
- Kamesh Raju K A, Chaubey A K, Amarnath Dileep and Mudholkar Abhay 2008 Morphotectonics of the Carlsberg Ridge between 62°20' and 66°20'E, northwest Indian Ocean; *Mar. Geol.* **252** 120–128.
- Kamesh Raju K A, Samudrala Kiranmai, Drolia R K, Amarnath D, Ramachandran R and Mudholkar A 2012 Segmentation and morphology of the Central Indian Ridge between 3°S and 11°S, Indian Ocean; *Tectonophysics* **554–557** 114–126.
- Karson J A 1987 Along-axis variations in seafloor spreading in the MARK area; *Nature* **328** 681–685.
- Kuo B Y and Forsyth D W 1988 Gravity anomalies of the ridge-transform system in the south Atlantic between 31 and 34.5°S: Upwelling centers and variations in crustal thickness; *Mar. Geophys. Res.* **10** 205–232.
- Lin J and Morgan J P 1992 The spreading rate dependence of three-dimensional mid-ocean ridge gravity structure; *J. Geophys. Res.* **19** 13–16.
- Lin J, Purdy G M, Schouten H, Sempere J C and Zervas C 1990 Evidence from gravity data for focused magmatic accretion along the Mid-Atlantic Ridge; *Nature* **344** 627–632.
- MacDonald K C 1982 Mid-ocean ridges: Fine scale tectonic volcanic and hydrothermal processes within the plate boundary zone; *Ann. Rev. Earth Planet. Sci. Lett.* **10** 155–190.
- MacDonald K C and Fox P J 1990 Mid ocean ridge; *Scientific American* **262(6)** 42–49.
- MacDonald K C, Scheirer D S and Carbotte S M 1991 Mid-Ocean Ridge: Discontinuities, segments and giant cracks; *Science* **253** 986–994.
- Maia M and Gente P 1998 Three-dimensional gravity and bathymetry analysis of the Mid-Atlantic Ridge between 20°N and 24°N: Flow geometry and temporal evolution of the segmentation; *J. Geophys. Res.* **103** 951–974.
- McKenzie D P and Sclater J G 1971 The evolution of the Indian Ocean since the Late Cretaceous; *Geophys. J. Roy. Astr. S.* **25** 437–528.
- Michael P J *et al.* 2003 Magmatic and amagmatic seafloor generation at the ultraslow-spreading Gakkel ridge, Arctic Ocean; *Nature* **423** 956–961.
- Neumann G A and Forsyth D W 1993 The paradox of the axial profile: Isostatic compensation along the axis of the Mid-Atlantic Ridge? *J. Geophys. Res.* **98** 17,891–17,910.
- Oldenburg D 1974 The inversion and interpretation of gravity anomalies; *Geophysics* **39** 526–536.
- Ortiz D G and Agarwal B N P 2005 3DINVER.M: A MATLAB program to invert the gravity anomaly over a 3-D horizontal density interface by Parker–Oldenburg's algorithm; *Comput. Geosci.* **31** 513–520.
- Pariso J E, Sempere J C and Rommevaux C 1995 Temporal and spatial variations in crustal accretion along the Mid-Atlantic Ridge (29°–31°30'N) over the last 10 MY: Implications from a three dimensional gravity study; *J. Geophys. Res.* **100** 17,781–17,794.
- Parker R L 1972 The rapid calculations of potential anomalies; *Geophys. J. Roy. Astr. Soc.* **31** 447–455.
- Phipps Morgan J and Chen Y J 1993 Dependence of ridge-axis morphology on magma supply and spreading rate; *Nature* **364** 706–708.
- Phipps Morgan J and Forsyth D W 1988 3-D flow and temperature perturbations due to a transform offset: effects on oceanic crustal and upper-mantle structure; *J. Geophys. Res.* **94** 2955–2966.
- Prince R A and Forsyth D W 1988 Horizontal extent of anomalous thin crust near the Vema Fracture Zone from the three-dimensional analysis of gravity anomalies; *J. Geophys. Res.* **93** 8051–8063.
- Rommevaux C, Deplus C, Patriat P and Sempere J C 1994 Three dimensional gravity study of the Mid-Atlantic Ridge: Evolution of the segmentation between 28° and 29°N during the last 10 m.y; *J. Geophys. Res.* **99** 3015–3029.
- Royer J Y and Sandwell D T 1989 Evolution of the eastern Indian Ocean since the Late Cretaceous – Constraints from geosat altimetry; *J. Geophys. Res.* **94** 13,755–13,782.
- Sandwell D T and Smith W H F 1997 Marine gravity anomaly from geosat and ERS-1 altimetry; *J. Geophys. Res.* **102** 10,039–10,054.
- Sauter D, Patriat P, Jestin C R, Cannat M, Brias A, Gallieni and Shipboard Scientific Party 2001 The Southwest Indian Ridge between 49°15'E and 57°E: Focused accretion and magma redistribution; *Earth Planet. Sci. Lett.* **192** 303–317.
- Scheirer D S and MacDonald K C 1993 Variation in cross-sectional area of the axial ridge along the East Pacific Rise: Evidence for the magmatic budget of a fast spreading center; *J. Geophys. Res.* **98** 7871–7885.
- Schlich R 1982 The Indian Ocean: Aseismic ridges, spreading centers, and oceanic basins; In: The Ocean Basins and Margins (eds) Nairn A E M and Stehli F G, vol. 6, *The Indian Ocean, Plenum*, New York, pp. 51–147.
- Sempère J C, Purdy G M and Schouten H 1990 The segmentation of the Mid-Atlantic Ridge between 24°N and 30°40'N; *Nature* **344** 427–431.
- Sempère J C, Lin J, Brown H S, Schouten H and Purdy G M 1993 Segmentation and morphotectonic variations along a slow-spreading center: The Mid-Atlantic Ridge (24°00'N–30°40'N); *Mar. Geophys. Res.* **15** 153–200.

- Sempère J C *et al.* 1995 The Mid-Atlantic Ridge between 29°N–31°31'N in the last 10 Ma; *Earth Planet. Sci. Lett.* **130** 45–55.
- Shaw P R 1992 Ridge segmentation, faulting and crustal thickness in the Atlantic Ocean; *Nature* **358** 490–493.
- Shaw P R and Lin J 1993 Causes and consequence of variations in faulting style at the Mid-Atlantic Ridge; *J. Geophys. Res.* **98** 21,839–21,851.
- Shaw W J and Lin J 1994 Three-dimensional modelling of thermo-mechanical structure of oceanic spreading centers: Effects of along-axis thickness variations associated with segmentation and hot spots (abstract); *EOS Trans. AGU* **75(16)**, Spring Meeting Suppl. **331**.
- Sinton J M and Detrick R S 1992 Mid-Ocean Ridge Magma Chambers; *J. Geophys. Res.* **97** 197–216.
- Smith D K and Cann J R 1993 Building the crust at the Mid-Atlantic Ridge; *Nature* **365** 707–715.
- Spudich P and Orcutt J 1980 A new look at the seismic velocity structure of the oceanic crust; *Rev. Geophys. Space Phys.* **18** 627–645.
- Tapponnier P and Francheteau J 1978 Necking of the lithosphere and the mechanics of slowly accreting plate boundaries; *J. Geophys. Res.* **83** 3955–3970.
- Tolstoy M, Harding A J and Orcutt J A 1993 Crustal thickness on the Mid-Atlantic Ridge bull's Eye gravity anomalies and focused accretion; *Science* **262** 726–729.
- Turcotte D L and Schubert G 2002 *Geodynamics*; 2nd edn; Cambridge Univ. Press, Cambridge, UK, 472p.
- Vine F J and Matthews D M 1963 Magnetic anomalies over ocean ridges; *Nature* **199** 947–949.
- van Wijk J W and Blackman D K 2005 Deformation of oceanic lithosphere near slow-spreading ridge discontinuities; *Tectonophys.* **407** 211–225.
- Wang T, Lin J, Tucholke B and Chen Y J 2011 Crustal thickness anomaly in the North Atlantic Ocean basin from gravity analysis; *Geochem. Geophys. Geosys.* **12** Q0AE02, doi: [10.1029/2010GC003402](https://doi.org/10.1029/2010GC003402).
- Wessel P and Smith W H F 1991 Free software helps map and display data; *EOS Trans. Am. Geophys. Union* **72** 445–446.

MS received 1 April 2016; revised 27 July 2016; accepted 16 August 2016

Corresponding editor: N PURNACHANDRA RAO